Impact of RbF post deposition treatment on CdS/CIGSe and Zn(O,S)/CIGSe interfaces – a comparative HAXPES study

Bünyamin Ümsür[1,*], Natalia Maticiuc[2], Tim Kodalle[2], Robert Wenisch[2], Isheta Majumdar[2], Yajie Wang[2], Hasan A. Yetkin[2,3], Tobias Bertram[2], Christian A. Kaufmann[2], Rutger Schlatmann[2,4], Iver Lauermann[2]

[1] Department of Physics, Yozgat Bozok University, 66100 Yozgat, Turkey

[2] Competence Center Photovoltaics Berlin (PVcomB) / Helmholtz Zentrum Berlin für Materialien und Energie (HZB), Schwarzschildstr. 3, 12489 Berlin, Germany

[3] Technology for Thin-Film Devices, Technische Universität Berlin, Einsteinufer Str. 25, 10587 Berlin, Germany

[4] Hochschule für Technik und Wirtschaft Berlin, Wilhelminenhofstr. 75a, 12459 Berlin, Germany

Abstract:

In conventional $Cu(In,Ga)Se_2$ (CIGSe) solar cells a chemical bath deposited CdS thin film is used as a buffer layer. However, it is desired to replace CdS due to the toxicity of cadmium and the rather narrow bandgap energy of CdS. Zn(O,S) is considered to be one of the most attractive candidates as an alternative, non-toxic buffer layer with a larger bandgap. This paper aims to compare the properties of the CdS/CIGSe and the Zn(O,S)/CIGSe interfaces depending on the absorber composition and the application of an RbF post deposition treatment (PDT). Synchrotron-based hard X-ray photoelectron spectroscopy revealed a strong correlation of Cd diffusion and concentration of V_{Cu} in CIGSe before the PDT. Additionally, the RbF-PDT enhanced the Cd diffusion into the CIGSe. On the other hand, it was found that Zn atoms are not as easily incorporated into the CIGSe as Cd atoms. As a result, we consider the formation of donor-like Zn_{Cu}^{+} defects at the interface to be less likely than the formation of Cd_{Cu}^{+} defects. Moreover, we observed that the Zn(O,S)/CIGSe interface is less sensitive to changes of the CIGSe composition and to the RbF-PDT compared to the CdS/CIGSe interface.

Keywords: Solar cells, CIGSe, RbF-PDT, Zn(O,S), CdS, interface, HAXPES

***Corresponding author:** Email: bunyamin.umsur@yobu.edu.tr

1. Introduction

Thin film solar cells based on polycrystalline Cu(In,Ga)Se_2 (CIGSe) chalcopyrite absorbers have recently reached a record power conversion efficiency of 23.35% [1], in league with polycrystalline silicon solar cells, which currently show a record efficiency of 24.4% [2]. Since the 20% efficiency threshold value was surpassed by using the so-called KF post deposition treatment (PDT) on CIGSe absorber layers [3], much effort has been made to reveal the beneficial effects of KF as well as the other heavy alkali-fluoride PDTs such as RbF or CsF [4–13]. As a result, the latest record efficiencies were reached by the application of RbF-PDT for the co-evaporated CIGSe [14] and CsF-PDT for sequentially sputtered/selenised CIGSe [1], respectively. Due to historical reasons chemical bath deposited (CBD) CdS thin films are still widely used as buffer layers in CIGSe solar cells. Therefore, the impact of alkali treatments on the properties of the CdS/CIGSe interface is studied in detail and it was shown that they can lead to a better coverage of CIGSe by CBD-CdS [15], a more homogeneous and a faster growth rate of CdS [16], enhanced Cd diffusion [17], accumulation of Rb at the CdS/CIGSe interface [10], formation of an $RbInSe_2$ compound at the interface [12], etc. However, because of the toxicity of Cd, the CdS buffer layer is desired to be eliminated from the cell structure. The Zn(O,S) buffer material is an attractive candidate due to its non-toxic nature and a larger, tunable band gap energy ($E_g^{CdS} \approx 2.4$ eV [18] and $E_g^{Zn(O,S)} \approx (3.4 \pm 0.2)$ eV [19]) reducing the parasitic absorption in the buffer layer. Therefore, research groups and industry recently increased their efforts to replace CdS by Zn(O,S). In fact, the latest record efficiencies were obtained using a Zn-based, Cd-free buffer layer in combination with the application of an alkali-PDT both in the laboratory scale [1] as well as in a module size of 30 cm x 30 cm [20]. However, the impact of such an alkali-PDT on the formation of the Zn(O,S)/CIGSe interface has not yet been systematically studied. It is crucial to understand the formation of this interface in order to optimize the buffer layer as well as the buffer/absorber interface. In this work we aim to compare the properties of CdS/CIGSe and Zn(O,S)/CIGSe interfaces under varied composition of the absorber and to investigate the impact of an RbF-PDT on the interface formation between CdS/CIGSe and Zn(O,S)/CIGSe.

Hard X-ray photoelectron spectroscopy (HAXPES) is a photoemission technique that employs X-rays with energies above 2000 eV for the excitation of photoelectrons. As a consequence, the HAXPES method provides a non-destructive analysis of buried films and interfaces. Therefore, we use HAXPES in this work as a powerful characterization method to examine the impact of the RbF-PDT on the CdS/CIGSe and Zn(O,S)/CIGSe interfaces.

2. Experimental details

2.1. Sample preparation

Cu(In,Ga)Se_2: Polycrystalline CIGSe thin film absorber layers were deposited on molybdenum coated soda lime glass (SLG) substrates (Sn-free side) by a modified three stage co-evaporation process. Details on this process are given in Ref. [21]. For the experiment in this work, two rather Cu-poor CIGSe samples and two CIGSe samples close-to-stoichiometry were grown on 5 cm x 5 cm large Mo coated SLG substrates with bulk compositions of [Cu]/([Ga]+[In]) (*CGI*) ≈ 0.80 and 0.95, respectively, and [Ga]/([Ga]+[In]) (*GGI*) ≈ 0.3 for both sample sets, as measured by X-ray fluorescence spectroscopy. For convenience, we will call the samples "Cu-poor" (*CGI* ≈ 0.80) and "Cu-rich" (*CGI* ≈ 0.95). The desired *CGI* was achieved by adjusting the duration of the third deposition stage of the co-evaporation, meaning that the Cu-poor samples are slightly thicker than the Cu-rich samples. For each composition, two deposition runs were performed: one with a subsequent in situ RbF-PDT and one without. After finishing the deposition of the absorber layers, the as deposited samples were stored in vacuum. The RbF-PDT was performed in the same ultra-high vacuum (UHV) co-evaporation chamber, directly after the CIGSe deposition, without a vacuum-break. In the presence of Se, RbF was evaporated onto the CIGSe for 10 min at a substrate temperature of 280 °C (see [22] for details regarding the RbF-PDT). One of the RbF treated and non-treated "Cu-poor" and "Cu-rich" CIGSe samples each was then cut to a size of 4 mm x 8 mm and covered with CdS and Zn(O,S) thin films as described in the following paragraph. The small size of the samples was required for the spectroscopic analyses. Therefore, the sample cutting and buffer deposition were performed right before the respective measurements.

CdS: Thin CdS films were deposited by chemical bath deposition (CBD) using 0.0189 M cadmium acetate dihydrate ($Cd(C_2H_3O_2)_2 \cdot 2H_2O$) in 11.25 ml aqueous NH_3(25%) and 0.9565 M thiourea (H_2NCSNH_2) in 100 ml water which were mixed together and filled up by distilled water to a total volume of 150 ml. A more detailed description of this process can be found elsewhere [23]. All four samples (Cu-poor, Cu-poor/RbF, Cu-rich and Cu-rich/RbF) were simultaneously dipped into the chemical bath for 50 s at 60 °C leading to circa 5 nm thick CdS films. An additional rinsing process was not applied to the samples before the CdS deposition. The large volume of the chemical bath (150 ml) in comparison to the sample size (4 mm x 8 mm) minimizes the risk of cross-contamination between the samples. As it can be seen also in the XPS survey spectra (**Fig. 2**), the cross-contamination is not an issue here. The same

argument is valid for the deposition of Zn(O,S) thin films, which is described in the following section.

Zn(O,S): Thin films of Zn(O,S) were deposited on top of the CIGSe films by CBD, where the entire amount of Zn^{2+} precursor ($ZnSO_4 \cdot 7\ H_2O$; [0.15 mol/l]) is mixed with thiourea (H_2NCSNH_2; [0.60 mol/l]) in an aqueous solution at 70-80 °C. An excess of ammonia (NH_3) was then added to the bath solution under constant stirring. A more detailed description of the CBD-Zn(O,S) process can be found in Ref. [24]. Four pieces of 4 mm x 8 mm sized samples, the similar ones as in the CdS deposition were simultaneously dipped into the chemical bath for 1 min at about 70 °C. The samples were not rinsed before the Zn(O,S) deposition. The deposition time was expected to be sufficient for depositing a sufficient amount of Zn(O,S) to cover the CIGSe surface and to allow the analysis of the Zn(O,S)/CIGSe interface. Although the final product of the present CBD method is an O- and H-containing zinc species, which are denoted as Zn(S,OH) and $Zn(O,S,OH)_x$ [25-27] , we will refer to the CBD-Zn(O,S) as ZnS for simplicity, just as in case of CdS. Another reason for this consideration is that an oxygen-free phase of ZnS is detected in the very early stage of CBD when using the similar process parameters [24].

Subsequent to the respective CBD of CdS and ZnS, the samples were rinsed with deionized water and dried in an ultra-pure nitrogen gas stream. They were finally transferred to the UHV based analysis system dedicated for hard X-ray photoelectron spectroscopy (HAXPES) using a small transport box flooded with nitrogen in order to minimize the impact of air exposure. However, all the samples were shortly exposed to air before entering the HAXPES load lock chamber.

A list of the samples under investigation is given together with a brief description in **Table S1** and is schematically depicted in **Fig. 1**. Comparison of the samples as shown with the arrows in **Fig. 1** will reveal the impact of RbF-PDT on the buffer/CIGSe interfaces for both CdS and ZnS buffer materials combined with two different absorber compositions.

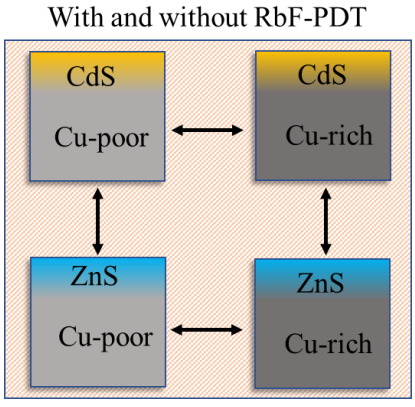

Fig. 1 Schematic representation of the samples (side view) under investigation. All samples are studied with and without RbF-PDT.

2.2. Sample characterization

The HAXPES measurements were performed at the HIKE end station [28], which is operated at the KMC-1 beamline [29] at the BESSY II synchrotron facility in Berlin, providing variable photon energies up to 12 keV. For the work presented in this paper, excitation energies of 2030 eV, 3000 eV, 4000 eV, 5000 eV, and 6000 eV were used. The analyzer at the HIKE end station consists of an R4000 hemispherical photoelectron spectrometer manufactured by Scienta Gammadata optimized for high kinetic energy. All spectra in this work were recorded at a constant pass energy of 200 eV. The X-ray beam was horizontally polarized and hit the sample in grazing incidence geometry under an angle of approximately 3° towards the surface. The generated photoelectrons were detected in the polarization plane perpendicular to the beam while the incident beam intensity was monitored with an N_2 ionization chamber and kept constant for all measurements (top-up mode of the storage ring with an average 298 mA ring current). The spot size of the beam on the sample under grazing incidence conditions was in the range of 0.1 mm in width and 1 mm in length, reducing the influence of surface roughness and inhomogeneity of the CdS and ZnS films on the accuracy of the measurements due to averaging effects. The entrance slit of the electron analyzer with 0.5 mm width was kept constant for all measurements.

X-ray fluorescence spectroscopy measurements were carried out using a Rigaku ZSX Primus II.

3. Results and discussion

HAXPES survey spectra of all the samples, recorded with an excitation energy of 3000 eV, are presented in **Fig. 2**. The spectra are plotted in the binding energy (E_B) range from 0 eV to 2500 eV. In the upper group of spectra, CdS related peaks, mainly Cd3d$_{5/2}$ at $E_B \approx 405$ eV and S1s ($E_B \approx 2470$ eV) are visible as expected. Similarly, in the bottom block of the spectra, the main core level peaks of the ZnS, namely Zn2p$_{3/2}$ ($E_B \approx 1022$ eV) and S1s can clearly be seen. In addition to the ZnS and CdS related peaks, photoelectron signals originating from the CIGSe absorber are also visible in all spectra in **Fig. 2** (E_B (Cu2p$_{3/2}$) ≈ 932 eV, E_B (In3d$_{5/2}$) ≈ 444 eV, E_B (Ga2p$_{3/2}$) ≈ 1118 eV, E_B (Se2p$_{3/2}$) ≈ 1433 eV). This is a direct indication that the thicknesses of the CdS and the ZnS films are limited to a few nanometers and the information depth of the

photoelectrons allows to record information from the underlying CIGSe absorber, the covering layers, and the interface between them. Although both the CdS and the ZnS films are comparably thin for the planned experiments, a quick comparison of the two sets of spectra shows that the ZnS layer attenuates the absorber related peaks more than CdS, implying a slightly thicker ZnS film.

In addition to the main constituent elements, oxygen and carbon are detectable on the samples due to the wet chemical deposition of ZnS and CdS films and the short air exposure after the CBD processes. Comparing the O1s peaks at $E_B \approx 532$ eV, samples with the ZnS buffer layer show higher signal intensity, possibly due to formation of an oxygen containing Zn(O,S) film. Also, the intensity of the C1s signal is higher in the case of the ZnS samples possibly attributed to the larger thickness of the ZnS layer.

At first glance, the spectra of the Cu-poor samples look very similar before and after PDT (black and red lines), indicating that the impact of RbF is not dramatic in the case of CdS/Cu-poor and ZnS/Cu-poor samples. On the other hand, comparison of the spectra of the Cu-rich samples shows a clear increase in $In3d_{5/2}$ and decrease in $Ga2p_{3/2}$ signals as a result of the RbF treatment in both cases (CdS/Cu-rich and ZnS/Cu-rich). Looking more closely at the $Cu2p_{3/2}$ signals, one would normally expect a higher signal intensity in the case of Cu-rich samples in comparison to the Cu-poor ones. This is true only for CdS covered samples, while after ZnS deposition they appear similar for Cu-poor and Cu-rich samples.

In **Fig. 2**, all spectra show similar HAXPES signal positions (E_B), implying a high quality and reproducible sample preparation. However, variation in the signal intensities indicates a change in composition at the CIGSe surface or at the interface region of CdS/CIGSe and ZnS/CIGSe as a result of the RbF-PDT or the type of the buffer material. These aspects are analyzed in the following using detailed HAXPES spectra of the core level signals.

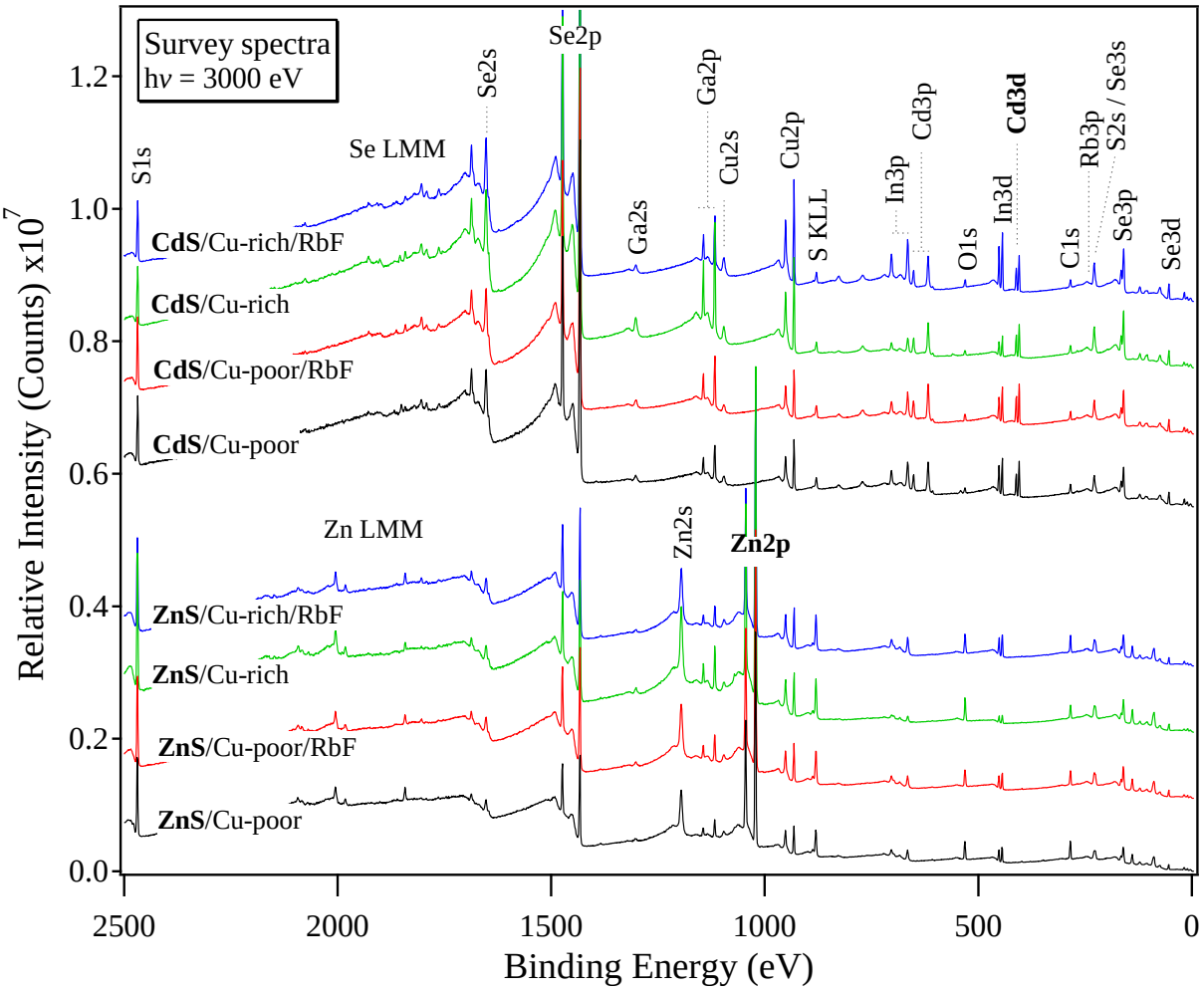

Fig. 2 XPS survey spectra of the ZnS- (lower group) and CdS- (upper group) covered CIGSe samples. Same color coding applies to both groups. Black: Cu-poor, red: Cu-poor/RbF-PDT, green: Cu-rich and blue: Cu-rich/RbF-PDT. Offsets between the spectra are added for clarity.

To evaluate the impact of the RbF-PDT and the type of the buffer material on the buffer/CIGSe interfaces, detailed spectra of the $Cu2p_{3/2}$, $In3d_{5/2}$, $Ga2p_{3/2}$, $Se2p_{3/2}$, $Cd3d_{5/2}$, $Zn2p_{3/2}$, and S1s orbitals were recorded at excitation energies of 2030 eV, 3000 eV, 4000 eV, 5000 eV and 6000 eV. Increasing excitation energies were applied in order to extend the information depth across the interfaces. These excitation energies correspond to a range of information depths (*ID*) from ~4 nm to ~24 nm, calculated using the equation $ID = 3 \cdot \lambda_{(CdS\ or\ ZnS)}$. In this equation, the inelastic mean free path (IMFP) for an element in the CdS material (λ_{CdS}) or in the ZnS material (λ_{ZnS}) were used depending on the type of the buffer material and calculated by the TPP-2M formula [30] using the QUASES code [31]. As the photoelectrons originating from the CIGSe material pass not only through the CdS or ZnS buffer materials but also through the CIGSe material, the calculated *ID* is considered as an approximation value of

the information depth. The validity of this approximation is briefly discussed in Supplementary Material with the help of some IMFP values listed in **Table S4**.

Fig. S1 exemplarily shows the detailed core level spectra, which were recorded at 3000 eV. For the quantitative analysis of some useful ratios out of the detailed spectra, the core level spectra were first corrected with respect to the $Au4f_{7/2}$ peak located at $E_B \approx 84.0$ eV [32]. A Shirley type background was then subtracted [32] and the spectra were integrated in order to determine the respective cumulative intensity for each line. All the line intensities were normalized to the corresponding inelastic mean free path λ [30,31], the transmission function of the analyzer T (provided by Gammadata Scienta), and the partial subshell photoionization cross-section $d\sigma/d\Omega$ as tabulated in Refs. [33,34]. The normalization procedure is performed in order to convert the integrated HAXPES line intensities into a "comparable form" to each other, since they depend on the photoelectron kinetic energy and the excitation energy. The application of the normalization procedure on the line intensities would result in atomic ratios of the constituent elements assuming their homogeneous distribution. In reality, elemental concentrations are depth-dependent. Therefore, we call the normalized core level line intensities as to have a "comparable form" and not absolute atomic concentration ratios. Using the normalized core level line intensities, relative intensities of the main elements Cu, In, Ga, Se, Cd (or Zn) and S are calculated (normalized to the sum of the intensities over all involved elements). The results are shown in **Fig. S2** and **S3** for the Cu-rich and Cu-poor samples, respectively. There, we omit the data recorded with 2030 eV excitation energy since the electrons in the S1s orbital cannot be excited at that energy. A rough comparison of the data in **Fig. S2** reveals that in the case of the Cu-rich CIGSe, the RbF-PDT leads to an overall decrease in Ga and increase in In concentrations, independent of the buffer type. An additional In enrichment towards the surface of the CdS/Cu-rich sample can be observed. Additionally, the RbF-PDT leads to a reduction of the Zn concentration throughout the analyzed depth of the ZnS/Cu-rich sample, whereas it slightly increases in case of the ZnS/Cu-poor sample in **Fig. S3**. Some relevant elemental ratios like *CGI*, *GGI* and [Zn, Cd]/[Cu]+[Zn, Cd] were calculated using the data in **Fig. S2** and **S3**.

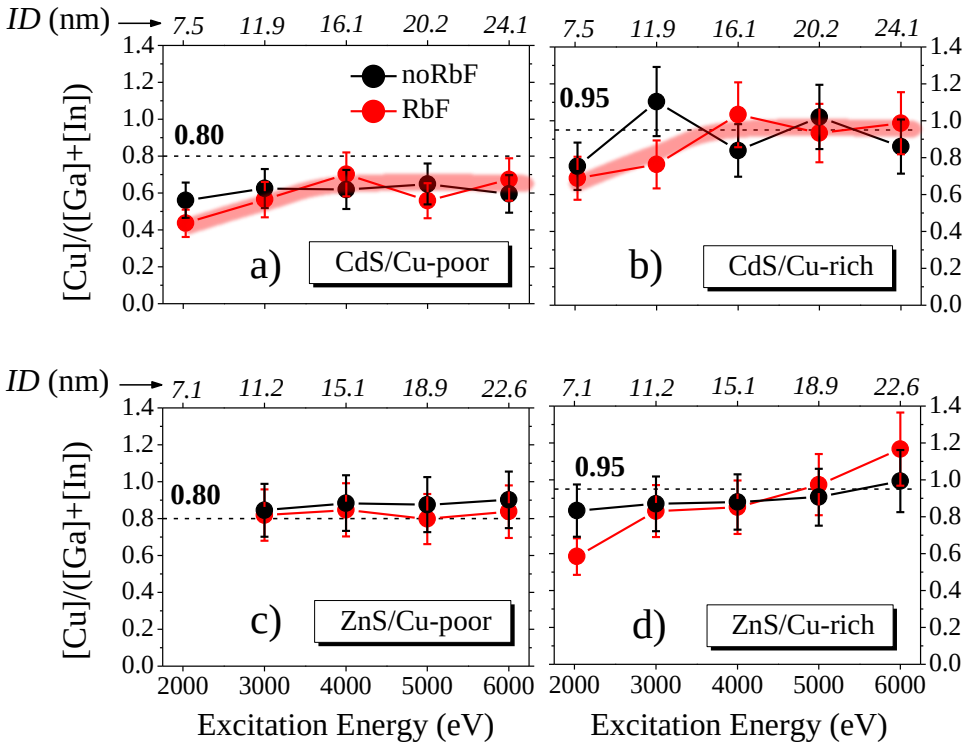

Fig. 3 *CGI* ratios of the a) CdS/Cu-poor, b) CdS/Cu-rich, c) ZnS/Cu-poor and d) ZnS/Cu-rich samples without (black) and with (red) RbF treatment as a function of excitation energy. Top axis shows the corresponding information depth. Dashed lines represent the nominal bulk values. Lines between data points are guides for the eyes only. The thicker red lines in a) and b) highlights the general trend of the data after RbF-PDT. The data points in c) at 2030 eV are missing because of an error in data acquisition.

Fig. 3 shows the *CGI* ratios of all the samples: a) CdS/Cu-poor, b) CdS/Cu-rich, c) ZnS/Cu-poor and d) ZnS/Cu-rich as a function of excitation energy. Black and red colored data points show the results before and after RbF-PDT, respectively. Dashed lines represent the nominal bulk values. The *ID*s for the corresponding *CGI* data given in the top axis of the graphs are calculated as the average value between the minimum and the maximum *ID* of $Cu2p_{3/2}$, $Ga2p_{3/2}$ and $In3d_{5/2}$ as explained above. One should keep in mind that the data presented here does not represent depth profiles. Namely the data does not correspond to a defined depth as shown with *ID*s, because at every *ID* the HAXPES signals contain contributions from the entire depth through which the photoelectrons travel. Therefore, the *CGI* ratio (as well as the other elemental ratios in **Fig. 4** and **Fig. 5**) vs. excitation energy (or *ID*) should be considered as a qualitative assessment of the elemental distribution. Nevertheless, the *ID*s are added to the respective graphs in order to give the reader an idea of how far we are probing into the surface.

The *CGI* ratio of the untreated CdS/Cu-poor sample presents an almost constant value of 0.6 for the investigated sample surface, only slightly increasing over the probed range of the excitation energy (**Fig. 3a**). In the case of the CdS/Cu-rich sample, the *CGI* values fluctuate around the bulk value (**Fig. 3b**). Nevertheless, the "more Cu-depleted" and the "less Cu-depleted" CIGSe surfaces are visible for the samples CdS/Cu-poor and CdS/Cu-rich, respectively, before the RbF treatment as it was similarly shown for the bare CIGSe samples without CdS [35]. Comparing the two samples, the *CGI* ratio of the Cu-poor sample appears to have, on average, 0.25 lower values within the probed depth compared to the Cu-rich sample. This value is approximately 0.1 higher than the difference in the bulk values indicated by the dashed lines. This means that the more pronounced under-stoichiometry of the Cu-poor samples seems to manifest in a strongly Cu-depleted surface rather than a fixed reduction of the *CGI* over the whole sample depth, which can be explained by the deposition procedure, as described in the section above. Furthermore, both untreated Cu-poor and Cu-rich samples would be expected to present a stronger Cu-depletion at the very-near surface than in the bulk [36]. When an RbF treatment was applied to the samples, this Cu-depletion at the very surface is enhanced in both samples (highlighted), while the *CGI* at higher excitation energies is unchanged.

A larger Cu-depletion range due to RbF-PDT was recently shown for a similar Cu-poor CIGSe sample without thin buffer film on top [35] and explained with the Cu migration towards the bulk of the absorber due to the formation of an $RbInSe_2$ secondary phase [4,8,9].

The *CGI* ratios of the ZnS covered samples are presented in **Fig. 3c** and **Fig. 3d**. The data points in **Fig. 3c** at 2030 eV are not shown because of an unfortunate error during data acquisition. The *CGI* of the ZnS/Cu-poor sample is homogeneously distributed around the bulk value. We would expect a more pronounced Cu deficiency in the case of ZnS deposited samples in comparison to the CdS ones due to the thicker ZnS. A thicker ZnS overlayer would result in a reduction of the probed depth in the CIGSe, namely in a shift of the analyzed depth towards the CIGSe surface-region. Thus, the contribution of the Cu-depleted region at the CIGSe surface onto the *CGI* ratio would be expected to be higher. However, within the error of the measurement, the *CGI* ratio for all four ZnS covered samples lies around its bulk value within the probed depth with the exception of the RbF-treated ZnS/Cu-rich sample, which shows a Cu-depletion at the surface. The interpretation of the depletion depends, however, mainly on the one data point taken at 2030 eV (**Fig. 3d**), while at 3000 eV there is only a slight tendency towards a Cu-depletion below the bulk value. We still consider this a true effect but we cannot exclude the remote possibility of an outlier data point. On the other hand, the data point at 6000 eV in the same graph, which also deviates strongly from the average *CGI* value, is most likely

an artefact because an abrupt increase in the *CGI* by around 20% when going from 5000 eV to 6000 eV is difficult to explain. The difference between the two extreme data points is that at 2030 eV we are most surface sensitive, i.e. a change of *CGI* at the very surface has a strong impact on the signal ratios, whereas at 6000 eV the signal is dominated by the composition of the entire volume between the surface and the electrons' inelastic mean free path. Changing the IMFP by increasing the excitation energy from 5000 eV to 6000 eV could therefore only lead to a comparatively small change in the signal ratios, even if we assume a sudden change in composition a few nm below the surface. The *CGI* decrease at the surface represents the result of an Rb-induced Cu depletion as it was discussed for the case of CdS above. It is interesting to note, however, that the surface Cu depletion is not so pronounced in the ZnS-buffered samples as in the CdS-buffered ones in case of Cu-poor samples (see **Fig S4** for a direct comparison). This might indicate to an interaction of the $RbInSe_2$ and the respective buffer layer, as will be discussed in more detail below.

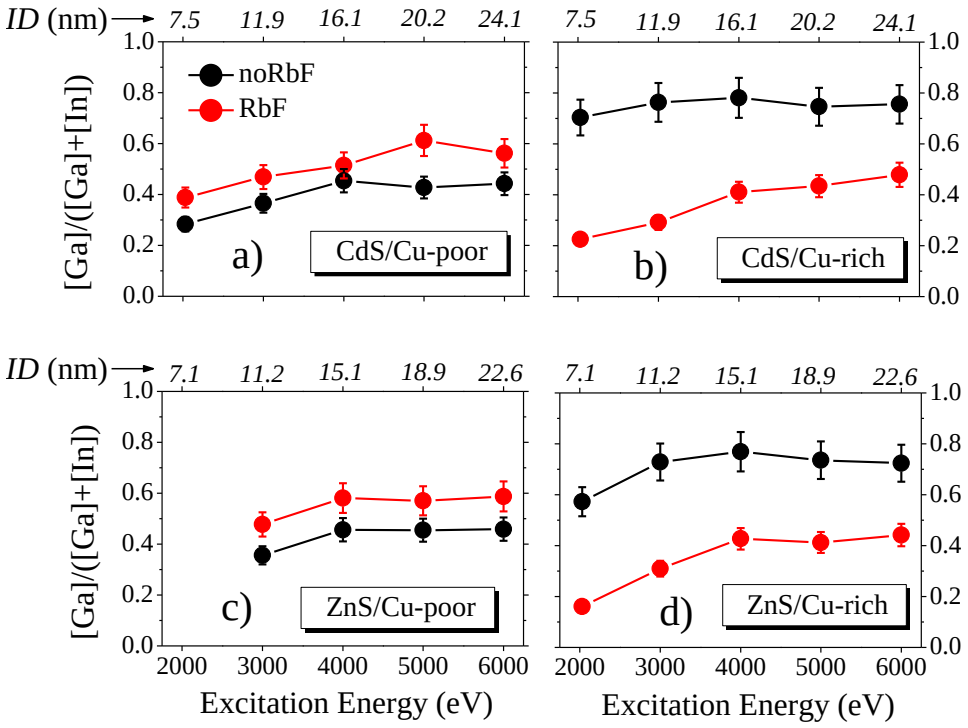

Fig. 4 *GGI* ratios of the a) CdS/Cu-poor, b) CdS/Cu-rich, c) ZnS/Cu-poor and d) ZnS/Cu-rich samples without (black) and with (red) RbF treatment as a function of excitation energy. Top axis shows the corresponding information depth. Lines between data points are guides for the eye only. The data points in c) at 2030 eV are missing because of an error in data acquisition.

Fig. 4 shows the *GGI* ratios as a function of excitation energy for the samples: a) CdS/Cu-poor, b) CdS/Cu-rich, c) ZnS/Cu-poor and d) ZnS/Cu-rich. Black and red colored data points show the results before and after RbF-PDT, respectively. The *ID*s for the corresponding *GGI* data are given in the top axis of the graphs. They are calculated as the average value between the *ID* of $Ga2p_{3/2}$ and $In3d_{5/2}$.

The *GGI* ratio of the non-treated CdS/Cu-poor sample starts at 0.3 for the lowest excitation energy and slightly increases up to 0.4 (**Fig. 4a**). Despite the small difference between the first and last values, the upward trend is still noticeable. The non-treated CdS/Cu-rich has an almost constant *GGI* value between 0.7 and 0.8 over the range of the used excitation energy (**Fig. 4b**). This is a very high value of *GGI*, which implies a Ga enrichment within the probed depth with respect to In. The effect of the RbF treatment on the *GGI* ratio strongly depends on the Cu-content. While it slightly increases the *GGI* of the CdS/Cu-poor sample over the investigated range of information depth, it strongly reduces the *GGI* of the CdS/Cu-rich sample. There, the *GGI* drops drastically from 0.7 down to 0.2 at 2030 eV excitation energy and it slightly increases to 0.5 with increasing excitation energy up to 6000 eV, but it remains well below its untreated counterpart.

Similar Ga-distributions at the very surface of samples with different Cu-content have been recently observed on buffer-free samples. It was concluded that this Ga-enrichment is related to the third stage of the co-evaporation process [35,37]. Furthermore, the *CGI*-dependent effect of the RbF-PDT on *GGI* was observed as well and explained with the formation of a GaF_3 secondary phase that is afterwards etched by an NH_3 solution [35].

The *GGI* values and their distribution of ZnS covered samples are shown in **Fig. 4c** and **Fig. 4d**. Clearly, ZnS covered samples show similar trends in *GGI* distribution as in the case of CdS covered and uncovered absorber layers [35]. Therefore, one can state that the variation in the *GGI* distribution can be dominantly attributed to the *CGI* and the RbF-PDT but not to the type of the buffer material.

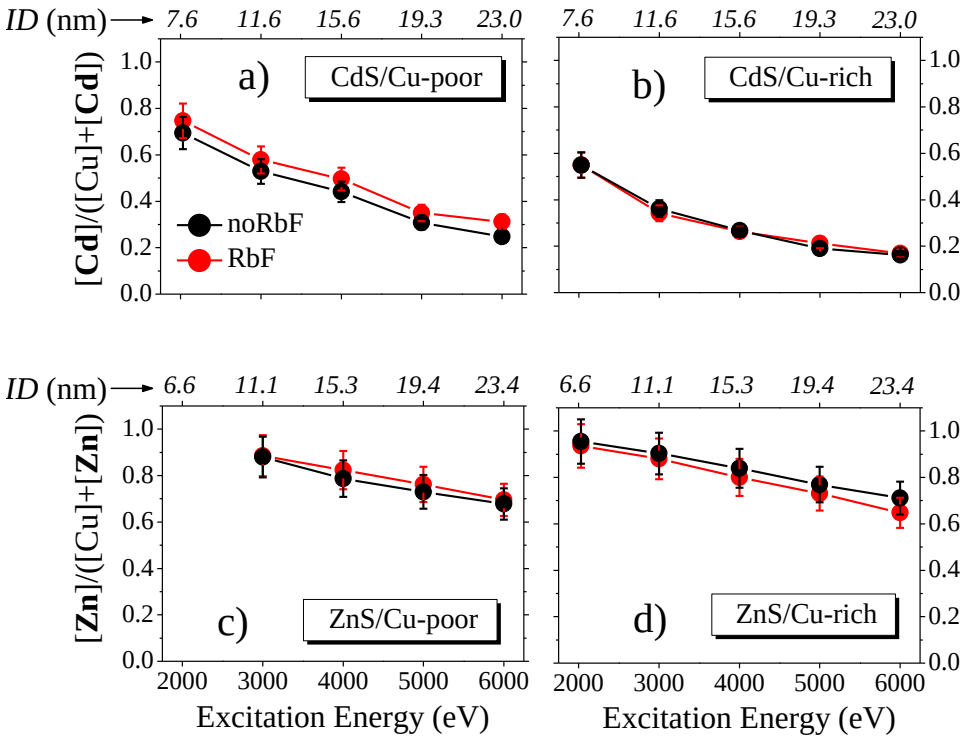

Fig. 5 [Cd] to [Cu]+[Cd] ratios for the a) CdS/Cu-poor and b) CdS/Cu-rich samples. [Zn] to [Cu]+[Zn] ratios for the c) ZnS/Cu-poor and d) ZnS/Cu-rich samples as a function of excitation energy. Top axis shows the corresponding information depth. Lines between data points are guides for the eye only. The data points in c) at 2030 eV are missing because of an error in data acquisition.

Fig. 5 shows the [Cd] to [Cu]+[Cd] ratios of the samples: a) CdS/Cu-poor, b) CdS/Cu-rich, and [Zn] to [Cu]+[Zn] ratios for the samples c) ZnS/Cu-poor and d) ZnS/Cu-rich as a function of excitation energy. Black and red colored data points show the results before and after RbF-PDT, respectively. The *ID*s for the corresponding ratios are given in the top axis of the graphs. They are calculated as the average value between the *ID*s of $Cu2p_{3/2}$ and $Cd3d_{5/2}$ (or $Zn2p_{3/2}$), respectively.

Fig. 5a and **Fig. 5b** show the [Cd] to [Cd]+[Cu] ratios with respect to applied X-ray excitation energy. In the case of the CdS/Cu-poor sample this ratio is overall higher than that of the CdS/Cu-rich regardless of the RbF-PDT (see **Fig S5** for a direct comparison of the data without RbF-PDT). It is widely known that Cd atoms substitute the vacant Cu sites in the CIGSe material and form Cd_{Cu} defects [38–41] or a $CdIn_2S_4$ mixed phase [42]. The higher relative amount of available Cu vacancies in the Cu-poor sample (when compared to the Cu-rich case) seems to trigger the Cd diffusion. This explains the higher Cd concentration in the case of the Cu-poor sample before the RbF-PDT. Moreover, the shape of the graph showing the

[Cd]/([Cd]+[Cu]) ratio over the excitation energy is similar for both Cu-poor and Cu-rich samples before RbF-PDT with only a constant difference of about 0.15 between the data. It means that if the Cd-Cu intermixing occurs as shown elsewhere [43,44], the rate of this intermixing is similar for both Cu-poor and Cu-rich samples. The RbF-PDT has almost no impact on the [Cd]/([Cd]+[Cu]) ratio in case of the CdS/Cu-rich sample. On the other hand, in case of the CdS/Cu-poor sample the application of RbF results in a constant upward shift of the [Cd]/([Cd]+[Cu]) ratio without changing its original shape. Even though this increase is not significant, it might indicate that the RbF-PDT leads to an extra exchange and/or intermixing between Cd and Cu at the CdS/Cu-poor interface. We observed a similar, and even stronger visible effect using a KF-PDT [45]. The reason why this Rb-enhanced Cd-diffusion does not occur in the case of the CdS/Cu-rich sample, may be connected with the interaction of Rb and Cu. It was previously shown that a $RbInSe_2$ surface layer forms on the CIGSe after a dedicated RbF-PDT [4,8,35]. The thickness of this $RbInSe_2$ layer was shown to be directly related to the V_{Cu} concentration, i.e. to the Cu-content of the CIGSe [9]. An indication to this can be seen in **Fig S6**, where a weak $Rb3p_{3/2}$ signal could be measured only at CdS/Cu-poor sample. Consequently, it is quite possible that the Rb atoms occupy some of the existing vacant Cu sites in the CIGSe and form Rb_{Cu} defects [46]. This idea is supported by the relatively low formation energy of the Rb_{Cu} defects (0.35 eV) [47]. Similar to the above case, the amount of Rb_{Cu} anti-site defects would then be proportional to the V_{Cu} concentration. In consequence, **Fig. 3** would imply that, Rb does not only occupy the available V_{Cu} but also replaces Cu at the very surface of the absorber layer. Therefore, the constant increase in the [Cd]/([Cd]+[Cu]) ratio might be due to an ion-exchange mechanism between Rb and Cd atoms, where Cd replaces Rb on Cu-sites (see proposed mechanism in **Fig. 6**). This mechanism is supported by the findings that the formation enthalpy of the Cd_{Cu} defect has a negative value in the order of -0.5 eV [48] and it is lower than that of the Rb_{Cu} defect [47]. In the case of Cu-rich CIGSe, the Cd concentration did not increase as a result of RbF-PDT, i.e. the Rb-diffusion into the CIGSe is less pronounced. This is in good agreement with the thinner $RbInSe_2$-layer observed on similar CIGSe absorbers when the *CGI* is increased [8].

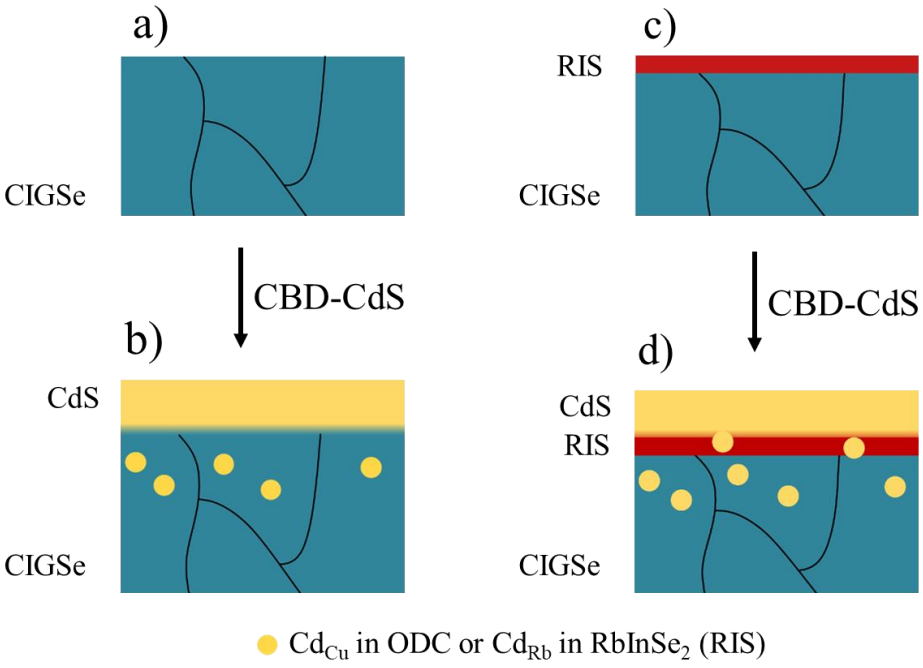

Fig. 6 Schematic view of the interface formation of Rb-free CIGSe (a-b) and RbF-treated CIGSe (c-d) during the chemical bath deposition of CdS. For a detailed description see the text.

Fig. 6 illustrates the proposed mechanism of the interface formation of Rb-free and RbF-treated CIGSe during the chemical bath deposition of CdS. In the Rb-free case, the starting point of the model is the polycrystalline CIGSe-layer (**Fig. 6a**), which exhibits a Cu-depleted surface. The amount of the Cu-depletion depends on the *CGI* of the absorber layer. During the CBD, the Cd atoms diffuse into this Cu-depleted surface layer forming Cd_{Cu} from the available V_{Cu} (**Fig. 6b**). In the case of RbF-treated CIGSe (**Fig. 6c**), the more Cu-deficient absorber material at the surface of the layer is partly consumed by the $RbInSe_2$-surface layer [49]. Accordingly, the in-diffusing Cd-atoms can occupy either V_{Cu} in the Cu-depleted CIGSe or Rb-sites in the $RbInSe_2$ (**Fig. 6d**), explaining the stronger Cd in-diffusion. Note that in both cases, the formation of additional secondary phases such as $CdIn_2(Se,S)_4$ is possible [42] and not in disagreement with our interpretation.

Fig. 5c and **Fig. 5d** show the [Zn] to [Zn]+[Cu] ratios with respect to excitation energy for the Cu-poor and Cu-rich samples, respectively. The [Zn]/([Zn]+[Cu]) ratios for both Cu-poor and Cu-rich samples are uniformly distributed having a similar shape and intensity over the probed depth before RbF-PDT. This result is fundamentally different from the results obtained for the CdS covered samples (**Fig. 5a** and **Fig. 5b**). This difference is demonstrated in more detail in **Fig S5**. It suggests that the incorporation of Zn atoms into V_{Cu} to form donor like Zn_{Cu}^{+} states does not occur as much as in the CdS-covered samples where Cd_{Cu}^{+} states are formed,

which is somewhat surprising given the fact that the formation energy of Cd_{Cu}^{+} was found to be slightly higher than the one of Zn_{Cu}^{+} [48]. We therefore assume that the hindered Zn-incorporation is due to kinetic reasons, i.e. the diffusion mechanism. This is supported by the fact that the amount of incorporated Zn is not directly proportional to the amount of available V_{Cu}, i.e. the Cu-content of the CIGSe, and therefore cannot be promoted by Rb. Considering the smaller ionic radius of Zn^{2+} versus Cd^{2+} (0.074 nm versus 0.095 nm), Zn is expected to move via an interstitial diffusion mechanism, whereas Cd tends to be more mobile via a Cu vacancy diffusion mechanism [50,51]. Such a difference in the diffusion mechanisms is supported by different experimental and theoretical reports from literature. There are some studies reporting Zn diffusion into the topmost region of CIGSe surface during the deposition process [52–54], whereas other studies reported negligible or no Zn diffusion during the CBD process [55–57]. Nakada et al. showed that the Zn diffusion into CIGSe would appear to be more difficult than for the case of Cd, and they observed almost no Zn diffusion into CIGSe before annealing, therefore an external "force" (like annealing) is needed for Zn atoms to diffuse and help in the formation of a *p-n* homojunction [57,58]. Additionally, Bastek et al. found a higher activation energy of Zn diffusion (~1.2 eV) in CIGSe compared to that of Cd (~1.0 eV) [55]. Therefore, it is expected that Cd penetrates deeper into the CIGSe absorber, whereas Zn is more confined to the near-surface region of the absorber [59] as we confirm in **Fig. 5**.

In order to confirm or reject the hypothesis, that the CdS forms a less stable buffer than ZnS, the experimental data is approximated with a simple two-layer model. The bottom layer is assumed to consist of CIGSe while the top layer consists of either CdS or ZnS. Changes in the buffer layers are assumed to reflect in the interdiffusion of buffer and CIGSe constituents.

In order to perform the simulation, the experimental data is corrected for the respective photoionization cross sections and the analyzer transmission function. For each excitation energy, the resulting data points are then normalized to their sum. This procedure results in excitation energy dependent apparent atomic ratios of the buffer and CIGSe elements. These data points reflect the depth-dependent attenuation of the photoelectrons passing through buffer and CIGSe. The depth dependent attenuation can then be calculated as described below for comparison with the experimental data. The depth attenuation of photoelectrons leaving a solid is described by the Beer-Lambert law

$$a(z) = exp\left(\frac{-z}{\lambda}\right),$$

where $a(z)$ is the depth attenuation factor, z is the depth in which the photoelectron was generated and λ is the IMFP. The total depth attenuation is obtained by integrating over all depths and results in $a_\infty = \lambda$ for a homogeneous medium. If the surface is covered by a thin layer of thickness d, the total depth attenuation for the surface layer becomes

$$a_{surf} = \int_0^d exp\left(\frac{-z}{\lambda_{surf}}\right) dz = \left[1 - exp\left(\frac{-d}{\lambda_{surf}}\right)\right] \lambda_{surf},$$

where λ_{surf} is the IMFP of the surface layer. The total depth attenuation of the lower layer assumed to be of infinite thickness (i.e. the bulk) becomes

$$a_{bulk} = exp\left(\frac{-d}{\lambda_{surf}}\right) \lambda_{bulk},$$

where λ_{bulk} is the IMFP of the lower layer. In both formulae, the angle under which the analyzer collects the photoelectrons from the sample surface, should be taken into account. The thickness d should therefore be corrected by a factor $(\cos \alpha)^{-1}$ where α denotes the angle of the analyzer versus the sample surface normal. In the present case, α=3°, resulting in a very small correction of < 0.2%. It is therefore omitted.

The simulation approximates the kinetic energy dependent IMFPs per element according to the TPP formula [60]. The excitation-dependent signals are then computed as $s^{el} = c_{surf}^{el} a_{surf}^{el} + c_{bulk}^{el} a_{bulk}^{el}$, where c^{el} and a^{el} are the element specific concentrations and attenuation factors respectively. The superscript el stands for the respective elements (Cu, Ga, In, Se, Zn/Cd, S). If an element appears both in bulk and surface layer, the surface and bulk signals are simply added together.

Finally, the depth attenuated, i.e. excitation energy dependent apparent atomic ratios are computed as

$$C_{app}^{el} = \frac{s^{el}}{\sum_{el} s^{el}}.$$

For brevity, they will be called apparent atomic ratios in the following.

The model is initialized with stoichiometric CdS or ZnS as the surface layer and Cu-poor CIGSe with a *CGI* of 0.8 or Cu-rich CIGSe with a *CGI* of 0.9. Both Cu-poor and Cu-rich CIGSe were initially modelled with *GGI*s of 0.3. During the simulation the concentrations in the layers were varied with the constraint $\sum_{el} c_y^{el} = 1$ (here y stands for either bulk or surface layer). Additionally, exchange between the layers was allowed for Zn/Cd, S, and Se. Additional tests with exchange of all elements between the layers did not yield significantly different results

and was abandoned due to the required excessive computational effort. The model was fitted to the data by minimizing the objective function

$$f(h\nu) = \sum_{el} \left(\frac{C_{app,exp}^{el} - C_{app,th}^{el}}{C_{app,exp}^{el}} \right)^2,$$

where the subscript *exp* and *th* refer to experimental and calculated values, respectively.

Due to the large numbers of fitting parameters, standard least-squares optimizations tend to perform poorly. Therefore, the differential evolution algorithm [61] was adopted as implemented within the SciPy package [62]. The reader is referred to the Supplementary Material of this manuscript for a discussion about the uncertainty estimation of this algorithm.

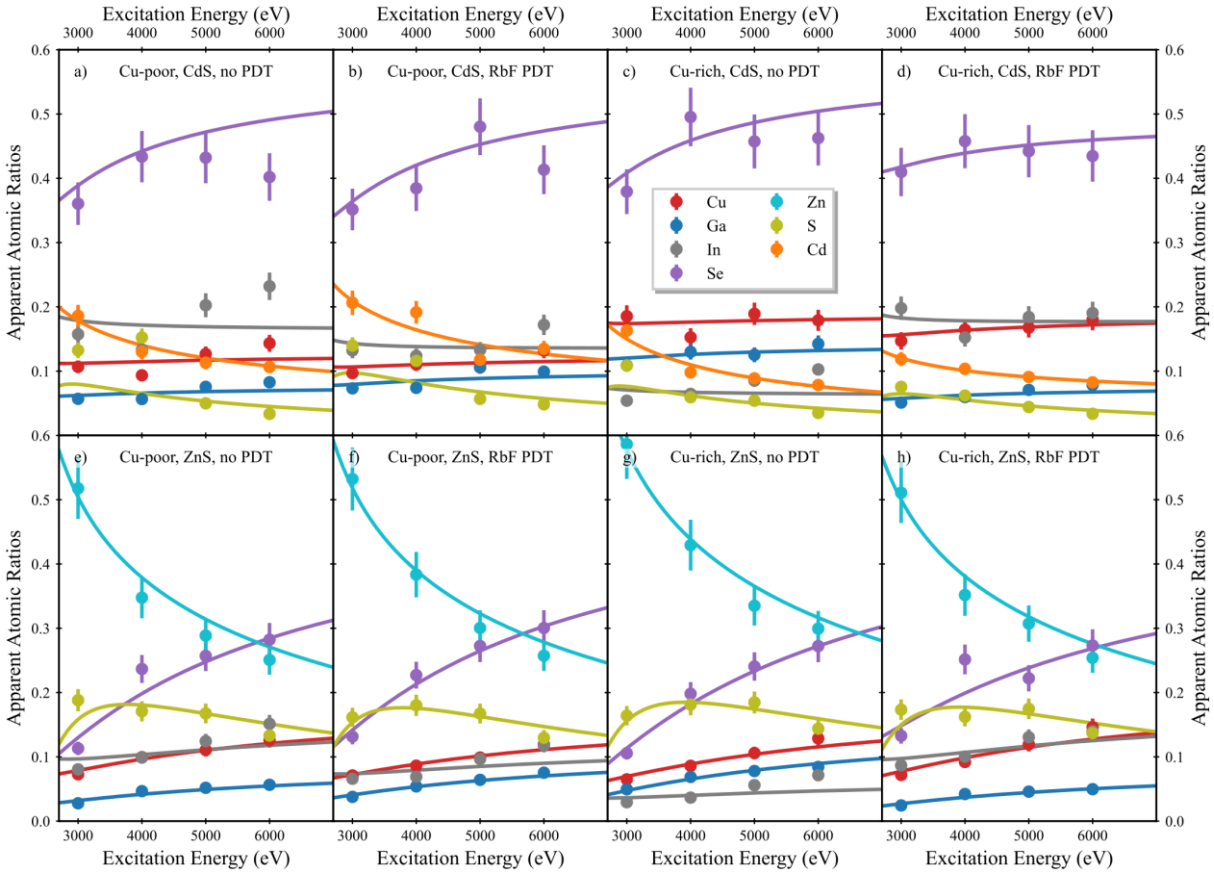

Fig. 7 The experimental data corrected for the photoionization cross sections and the analyzer transmission but not the depth attenuation (dots) superimposed with the fitted curves from the two-layer model. The panels a)-d) show the results for the samples with CdS buffer under various conditions (as indicated) while the panels e)-h) show the corresponding results for the samples with ZnS buffer. Error bars smaller than the marker are not shown. The legend in panel c) also applies to all other panels.

Applying the two-layer model to the experimental data using the fitting procedure described above yields apparent atomic ratio curves as shown in **Fig. 7**. In order to obtain comparable values, the 2030 eV excitation energy had to be omitted, as the S1s peak used for the S quantification has a BE of 2469.4 eV.

While the overall fit is satisfactory in most cases, the agreement with the S data point at 3000 eV is usually poor. This is due to the very high BE of the S1s peak. At the resulting low KE, both the cross section and the IMFP are changing rapidly, increasing the uncertainty. The apparent In concentrations for 5000 and 6000 eV of excitation energy are underestimated for both Cu-poor samples with CdS buffer. This might indicate a steep In concentration gradient in the CIGSe absorber near the interface not covered by the simple two-layer model with constant atomic ratios.

The model fit to the experimental data, results in *CGI* and *GGI* values (**Table S3**) in good agreement with the analysis presented above (**Fig. 3 and Fig. 4**). The composition of the CdS buffer is calculated to be close to stoichiometric (**Table S2**) while the ZnS buffers show lack in S. This may be explained by the presence of O and OH groups as residues from the deposition process.

Table 1 The concentrations of buffer elements in the modelled CIGSe layer. Additionally, also the modelled concentration of Se in the buffer is shown. The thicknesses are given in Å and the concentrations in %.

	CdS				ZnS			
	Cu-poor		Cu-rich		Cu-poor		Cu-rich	
	no RbF	RbF	no RbF	RbF	no RbF	RbF	no RbF	RbF
Buffer thickness	8±2	9±2	8±3	9±4	38±5	38±6	44±6	42±6
S in CIGSe	0	0	0	0	0	0	0	0
Cd in CIGSe	5±3	6±3	1±2	5±2	-	-	-	-
Zn in CIGSe	-	-	-	-	0	0	0	0
Se in buffer	2±10	1±5	6±18	43±18	0.0±1.2	1±3	1±2	6±4

As low buffer stability is expected to be related to in-diffusion of buffer elements into the CIGSe absorber, we examine the concentrations of S, Cd and Zn in the CIGSe absorber. Due to the chemical similarity of S and Se we also consider Se diffusion into the buffer layer. **Table 1** lists the resulting contaminant concentrations and the buffer thickness. The buffer thickness is found to be 8-9 Å for CdS buffers while the ZnS buffer layers show buffer thicknesses of 38-

44 Å. For all the samples with CdS buffer, Cd is found in the CIGSe layer, while for the samples with a ZnS buffer no Zn is ascribed to the lower layer. In no case is S found in the CIGSe layer. Generally, no Se or only small amounts thereof are found in the buffer layer with the exception of the Cu-rich RbF-treated samples. Here, larger amounts of Se are attributed to the top layer by the modelling procedure. In the case of the ZnS-buffer sample 6% of Se are found in the top layer while an enormous 43% are found for the CdS sample. The latter result seems rather unrealistic and may either stem from a spuriously large Se signal at 3000 eV excitation or from a Se-rich layer at the surface or the interface perhaps induced by the RbF treatment. The latter seems a likely explanation, as all samples except for the present two show excess Se in the CIGSe layer (see **Table S2** in SI). In this case, the high percentage value reflects the much lower thickness of the CdS buffer (9 Å, **Table 1**) compared to ZnS (42 Å, **Table 1**), the percentage needs to be much higher to account for a comparable quantity of Se.

The results presented above indicate a more stable and well-defined interface of the ZnS buffer on the CIGSe layer.

4. Conclusions

The properties of CdS and ZnS films formed on the CIGSe absorber and their corresponding interfaces are influenced by the CIGSe composition and RbF-PDT. The relationship between Cd diffusion and V_{Cu} availability was once more proved to govern the change at the CIGSe surface. The higher the V_{Cu} concentration in CIGSe is, the more Cd diffuses into the absorber. The application of the RbF-PDT leads to an increased Cd diffusion in the case of CIGSe with *CGI*=0.80. This is attributed to the Rb-Cd exchange mechanism in the $RbInSe_2$ compound and the formation of a (Cu,Cd)-In-S-Se mixed compound at the CdS/CIGSe interface, accompanied by the incorporation of Cd into the remaining V_{Cu} sites in the matrix. On the other hand, the interface between CdS and CIGSe with lower V_{Cu} concentration (*CGI*=0.95) is not affected by the RbF-PDT in terms of Cd incorporation. We also found that the incorporation of Zn atoms into the CIGSe does not occur as much as Cd atoms during the chemical bath deposition, i.e. the donor like Zn_{Cu}^{+} states do not form as easily as the Cd_{Cu}^{+} states. The available V_{Cu} concentration and RbF-PDT have limited effects on the ZnS/CIGSe interface in comparison to its CdS counterpart. The results that we obtained by applying a two-layer model go along successfully with the experimental data and further prove our hypothesis that the ZnS buffer layer forms a more stable and well-defined interface with CIGSe. Finally, our findings indicate that the variation in the *GGI* distribution at the interface

between the CdS or ZnS buffer and CIGSe can be attributed to the RbF-PDT and does not depend on the type of the buffer material.

Acknowledgments

The authors thank HZB for the allocation of synchrotron radiation beam time (172-05557-ST/R) and Dr. R. Félix for support during the measurements. The financial support by the German Federal Ministry for Economic Affairs and Energy in the frame of the speedCIGS project (contract number 0334095E) is also thankfully acknowledged. H.A. Yetkin gratefully acknowledges the financial support of the Ministry of National Education of the Republic of Turkey.

References

[1] M. Nakamura, K. Yamaguchi, Y. Kimoto, Y. Yasaki, T. Kato, H. Sugimoto, Cd-Free Cu(In,Ga)(Se,S)$_2$ thin-film solar cell with record efficiency of 23.35%, IEEE J. Photovoltaics. 9 (2019) 1863–1867.

[2] M. Green, E. Dunlop, J. Hohl-Ebinger, M. Yoshita, N. Kopidakis, X. Hao, Solar cell efficiency tables (version 57), Prog. Photovoltaics Res. Appl. 29 (2021) 3–15.

[3] A. Chirilă, P. Reinhard, F. Pianezzi, P. Bloesch, A.R. Uhl, C. Fella, L. Kranz, D. Keller, C. Gretener, H. Hagendorfer, D. Jaeger, R. Erni, S. Nishiwaki, S. Buecheler, A.N. Tiwari, Potassium-induced surface modification of Cu(In,Ga)Se$_2$ thin films for high-efficiency solar cells., Nat. Mater. 12 (2013) 1107–1111.

[4] N. Taguchi, S. Tanaka, S. Ishizuka, Direct insights into RbInSe$_2$ formation at Cu(In,Ga)Se2 thin film surface with RbF post deposition treatment, Appl. Phys. Lett. 113 (2018).

[5] E. Avancini, R. Carron, T.P. Weiss, C. Andres, M. Bürki, C. Schreiner, R. Figi, Y.E. Romanyuk, S. Buecheler, A.N. Tiwari, Effects of Rubidium Fluoride and Potassium Fluoride Postdeposition Treatments on Cu(In,Ga)Se$_2$ Thin Films and Solar Cell Performance, Chem. Mater. 29 (2017) 9695–9704.

[6] R. Wuerz, W. Hempel, P. Jackson, Diffusion of Rb in polycrystalline Cu(In,Ga)Se$_2$ layers and effect of Rb on solar cell parameters of Cu(In,Ga)Se$_2$ thin-film solar cells, J. Appl. Phys. 124 (2018) 0–14.

[7] P. Schöppe, S. Schönherr, R. Wuerz, W. Wisniewski, G. Martínez-Criado, M. Ritzer, K. Ritter, C. Ronning, C.S. Schnohr, Rubidium segregation at random grain boundaries in

$Cu(In,Ga)Se_2$ absorbers, Nano Energy. 42 (2017) 307–313.

[8] N. Maticiuc, T. Kodalle, J. Lauche, R. Wenisch, T. Bertram, C.A. Kaufmann, I. Lauermann, In vacuo XPS investigation of $Cu(In,Ga)Se_2$ surface after RbF post-deposition treatment, Thin Solid Films. 665 (2018) 143–147.

[9] T. Kodalle, T. Bertram, R. Schlatmann, C.A. Kaufmann, Effectiveness of an RbF Post Deposition Treatment of CIGS Solar Cells in Dependence on the Cu Content of the Absorber Layer, IEEE J. Photovoltaics. 9 (2019) 1839–1845.

[10] M. Raghuwanshi, A. Vilalta-Clemente, C. Castro, S. Duguay, E. Cadel, P. Jackson, D. Hariskos, W. Witte, P. Pareige, Influence of RbF post deposition treatment on heterojunction and grain boundaries in high efficient (21.1%) $Cu(In,Ga)Se_2$ solar cells, Nano Energy. 60 (2019) 103–110.

[11] D. Hauschild, D. Kreikemeyer-Lorenzo, P. Jackson, T.M. Friedlmeier, D. Hariskos, F. Reinert, M. Powalla, C. Heske, L. Weinhardt, Impact of a RbF Postdeposition Treatment on the Electronic Structure of the CdS/$Cu(In,Ga)Se_2$ Heterojunction in High-Efficiency Thin-Film Solar Cells, ACS Energy Lett. 2 (2017) 2383–2387.

[12] S. Ishizuka, N. Taguchi, P.J. Fons, Similarities and Critical Differences in Heavy Alkali-Metal Rubidium and Cesium Effects on Chalcopyrite $Cu(In,Ga)Se_2$ Thin-Film Solar Cells, J. Phys. Chem. C. 123 (2019) 17757–17764.

[13] S. Ishizuka, N. Taguchi, J. Nishinaga, Y. Kamikawa, S. Tanaka, H. Shibata, Group III elemental composition dependence of RbF postdeposition treatment effects on $Cu(In,Ga)Se_2$ thin films and solar cells, J. Phys. Chem. C. 122 (2018) 3809–3817.

[14] P. Jackson, R. Wuerz, D. Hariskos, E. Lotter, W. Witte, M. Powalla, Effects of heavy alkali elements in $Cu(In,Ga)Se_2$ solar cells with efficiencies up to 22.6%, Phys. Status Solidi (RRL). (2016) 1–4.

[15] T. Kodalle, L. Choubrac, L. Arzel, R. Schlatmann, N. Barreau, C.A. Kaufmann, Effects of KF and RbF post deposition treatments on the growth of the CdS buffer layer on CIGS thin films - a comparative study, Sol. Energy Mater. Sol. Cells. 200 (2019) 109997.

[16] T.M. Friedlmeier, P. Jackson, D. Kreikemeyer-lorenzo, D. Hauschild, O. Kiowski, D. Hariskos, L. Weinhardt, C. Heske, M. Powalla, A Closer Look at Initial CdS Growth on High-Efficiency $Cu(In,Ga)Se_2$ Absorbers Using Surface-Sensitive Methods, IEEE 43rd Photovolt. Spec. Conf. (2016) 0457–0461.

[17] B. Ümsür, W. Calvet, A. Steigert, I. Lauermann, M. Gorgoi, K. Prietzel, D. Greiner, C.A. Kaufmann, T. Unold, M.C. Lux-Steiner, Investigation of the potassium fluoride post deposition treatment on the CIGSe/CdS interface using hard X-ray photoemission

spectroscopy – a comparative study, Phys. Chem. Chem. Phys. 18 (2016) 14129–14138.

[18] M. Ichimura, F. Goto, E. Arai, Structural and optical characterization of CdS films grown by photochemical deposition, J. Appl. Phys. 85 (1999) 7411–7417.

[19] B.K. Meyer, A. Polity, B. Farangis, Y. He, D. Hasselkamp, T. Krämer, C. Wang, Structural properties and bandgap bowing of $ZnO_{1-x}S_x$ thin films deposited by reactive sputtering, Appl. Phys. Lett. 85 (2004) 4929–4931.

[20] https://www.avancis.de/en/avancis-achieves-new-efficiency-record-for-cigs-solar-modules/, date of access, 30 March. (2021).

[21] C.A. Kaufmann, A. Neisser, R. Klenk, R. Scheer, Transfer of $Cu(In,Ga)Se_2$ thin film solar cells to flexible substrates using an in situ process control, Thin Solid Films. 480–481 (2005) 515–519.

[22] T. Kodalle, M.D. Heinemann, D. Greiner, H.A. Yetkin, M. Klupsch, C. Li, P.A. van Aken, I. Lauermann, R. Schlatmann, C.A. Kaufmann, Elucidating the Mechanism of an RbF Post Deposition Treatment in CIGS Thin Film Solar Cells, Sol. RRL. 1800156 (2018) 1800156.

[23] B. Ümsür, Surface Engineering of $Cu(In,Ga)Se_2$ by KF and CdS – a Study by High-Energy Photoemission Spectroscopy, PhD Thesis, Freie Univ. Berlin. (2017).

[24] A. Ennaoui, M. Bär, J. Klaer, T. Kropp, R. Saez-Araoz, M.C. Lux-Steiner, Highly-efficient Cd-free $CuInS_2$ Thin-film Solar Cells and Mini-modules with Zn(S,O) Buffer Layers Prepared by an Alternative Chemical Bath Process, Prog. Photovoltaics Res. Appl. 14 (2006) 499–511.

[25] A. Ennaoui, W. Eisele, M. Lux-Steiner, T.P. Niesen, F. Karg, Highly efficient $Cu(Ga,In)(S,Se)_2$ thin film solar cells with zinc-compound buffer layers, Thin Solid Films. 431–432 (2003) 335–339.

[26] K. Kushiya, M. Ohshita, I. Hara, Y. Tanaka, B. Sang, Y. Nagoya, M. Tachiyuki, O. Yamase, Yield issues on the fabrication of 30 cm × 30 cm-sized $Cu(In,Ga)Se_2$-based thin-film modules, Sol. Energy Mater. Sol. Cells. 75 (2003) 171–178.

[27] M. Bär, A. Ennaoui, J. Klaer, T. Kropp, R. Sáez-araoz, Formation of a ZnS/Zn(S,O) bilayer buffer on $CuInS_2$ thin film solar cell absorbers by chemical bath deposition, J. Appl. Phys. 99 (2006) 123503.

[28] M. Gorgoi, S. Svensson, F. Schäfers, G. Öhrwall, M. Mertin, P. Bressler, O. Karis, H. Siegbahn, A. Sandell, H. Rensmo, W. Doherty, C. Jung, W. Braun, W. Eberhardt, The high kinetic energy photoelectron spectroscopy facility at BESSY progress and first results, Nucl. Instruments Methods Phys. Res. A. 601 (2009) 48–53.

[29] F. Schaefers, M. Mertin, M. Gorgoi, KMC-1: A high resolution and high flux soft x-ray beamline at BESSY, Rev. Sci. Instrum. 78 (2007) 123102.

[30] S. Tanuma, C.J. Powell, D.R. Penn, Calculations of Electron Inelastic Mean Free Paths., Surf. Interface Anal. 21 (1993) 165–176.

[31] S. Tougaard, QUASES-IMFP-TPP2M code for the calculation of the inelastic mean free path, Version 2.2. http://www.quases.com, 2002.

[32] D. Briggs, M.P. Seah, Practical Surface Analysis, John Wiley & Sons, Chichester, 1983.

[33] M.B. Trzhaskovskaya, V.I. Nefedov, V.G. Yarzhemsky, Photoelectron angular distribution parameters for elements Z=1 to Z=54 in the photoelectron energy range 100–5000 eV, At. Data Nucl. Data Tables. 77 (2001) 97–159.

[34] M.B. Trzhaskovskaya, V.I. Nefedov, V.G. Yarzhemsky, Photoelectron angular distribution parameters for elements Z=55 to Z=100 in the photoelectron energy range 100–5000 eV, At. Data Nucl. Data Tables. 82 (2002) 257–311.

[35] N. Maticiuc, T. Kodalle, B. Ümsür, T. Bertram, R. Wenisch, Yajie Wang, I. Majumdar, H.A. Yetkin, D. Abou-Ras, N. Schäfer, C.A. Kaufmann, R. Schlatmann, I. Lauermann, Depth-resolved analysis of the effect of RbF post deposition treatment on CIGSe with two different Cu concentrations, Sol. Energy Mater. Sol. Cells. 226 (2021) 111071.

[36] H. Mönig, C.H. Fischer, A. Grimm, B. Johnson, C.A. Kaufmann, R. Caballero, I. Lauermann, M.C. Lux-Steiner, Surface Cu-depletion of Cu(In,Ga)Se_2 thin films: Further experimental evidence for a defect-induced surface reconstruction, J. Appl. Phys. 107 (2010).

[37] H. Rodriguez-Alvarez, R. Mainz, S. Sadewasser, A one-dimensional Fickian model to predict the Ga depth profiles in three-stage Cu(In,Ga)Se_2, J. Appl. Phys. 115 (2014).

[38] J. Kiss, T. Gruhn, G. Roma, C. Felser, Theoretical study on the structure and energetics of Cd insertion and Cu depletion of $CuIn5Se_8$, J. Phys. Chem. C. 117 (2013) 10892–10900.

[39] T. Nakada, A. Kunioka, Direct evidence of Cd diffusion into Cu(In,Ga)Se_2 thin films during chemical-bath deposition process of CdS films, Appl. Phys. Lett. 74 (1999) 2444.

[40] D. Liao, A. Rockett, Cd doping at the $CuInSe_2$/CdS heterojunction, J. Appl. Phys. 93 (2003) 9380.

[41] H.A. Yetkin, T. Kodalle, T. Bertram, A. Villanueva-Tovar, M. Rusu, R. Klenk, B. Szyszka, R. Schlatmann, C.A. Kaufmann, Decay mechanisms in CdS-buffered Cu(In,Ga)Se_2 thin-film solar cells after exposure to thermal stress: Understanding the role of Na, Prog. Photovoltaics Res. Appl. (2021) 1–20.

[42] N. Barreau, A. Frelon, T. Lepetit, E. Gautron, N. Gautier, R. Ribeiro-Andrade, N. Nicoara, S. Sadewasser, P. Zabierowski, L. Arzel, L. Choubrac, S. Harel, C. Deudon, C. Latouche, S. Jobic, M. Caldes, L. Assmann, P. Tsoulka, E. V. Péan, J. Lorthioir, F. Geschier, I. Braems, M. Moret, O. Briot, G. Ouvrard, High Efficiency Solar Cell Based on Full PVD Processed Cu(In,Ga)Se_2/$CdIn_2S_4$ Heterojunction, Sol. RRL. 1 (2017) 1700140.

[43] S.M. Park, T.G. Kim, Y.D. Chung, D.-H. Cho, J. Kim, K.J. Kim, Y. Yi, J.W. Kim, Junction formation at the interface of CdS/$CuIn_xGa_{(1-x)}Se_2$, J. Phys. D. Appl. Phys. 47 (2014) 345302.

[44] X. He, T. Paulauskas, P. Ercius, J. Varley, J. Bailey, G. Zapalac, D. Poplavskyy, N. Mackie, A. Bayman, D. Spaulding, R. Klie, V. Lordi, A. Rockett, Cd doping at PVD-CdS/$CuInGaSe_2$ heterojunctions, Sol. Energy Mater. Sol. Cells. 164 (2017) 128–134.

[45] B. Ümsür, W. Calvet, A. Steigert, I. Lauermann, M. Gorgoi, K. Prietzel, D. Greiner, C.A. Kaufmann, T. Unold, M.C. Lux-Steiner, Investigation of the potassium fluoride post deposition treatment on the CIGSe/CdS interface using hard X-ray photoemission spectroscopy – a comparative study, Phys. Chem. Chem. Phys. 18 (2016) 14129–14138.

[46] F. Pianezzi, P. Reinhard, A. Chirilă, B. Bissig, S. Nishiwaki, S. Buecheler, A.N. Tiwari, Unveiling the effects of post-deposition treatment with different alkaline elements on the electronic properties of CIGS thin film solar cells., Phys. Chem. Chem. Phys. 16 (2014) 8843.

[47] I. Majumdar, S.K. Sahoo, V. Parvan, H. Mirhosseini, B. Chacko, Y. Wang, D. Greiner, T.D. Kühne, R. Schlatmann, I. Lauermann, Effects of KF and RbF treatments on Cu(In,Ga)Se_2-based solar cells: A combined photoelectron spectroscopy and DFT study, Appl. Surf. Sci. 538 (2021) 148085.

[48] C. Persson, Y.J. Zhao, S. Lany, A. Zunger, n-Type doping of $CuInSe_2$ and $CuGaSe_2$, Phys. Rev. B - Condens. Matter Mater. Phys. 72 (2005) 1–14.

[49] T. Kodalle, L. Choubrac, L. Arzel, R. Schlatmann, N. Barreau, C.A. Kaufmann, Effects of KF and RbF post deposition treatments on the growth of the CdS buffer layer on CIGS thin films - a comparative study, Sol. Energy Mater. Sol. Cells. 200 (2019) 109997.

[50] J. Bastek, N.A. Stolwijk, R. Wuerz, A. Eicke, J. Albert, S. Sadewasser, Zinc diffusion in polycrystalline Cu(In,Ga)Se_2 and single-crystal $CuInSe_2$ layers, Appl. Phys. Lett. 101 (2012) 2012–2015.

[51] N.J. Biderman, R. Sundaramoorthy, P. Haldar, J.R. Lloyd, Dissociative diffusion mechanism in vacancy-rich materials according to mass action kinetics, AIP Adv.

055211 (2016) 0–18.

[52] F. Erfurth, B. Hußmann, A. Schöll, F. Reinert, A. Grimm, F. Erfurth, B. Hußmann, A. Schöll, F. Reinert, A. Grimm, I. Lauermann, M. Bär, Chemical structure of the $(Zn_{1-x},Mg_x)O/CuIn(S,Se)_2$ interface in thin film solar cells, Appl. Phys. Lett. 95 (2009) 122104.

[53] O. Cojocaru-Miredin, Y. Fu, A. Kostka, Interface engineering and characterization at the atomic-scale of pure and mixed ion layer gas reaction buffer layers in chalcopyrite thin-film solar cells, Prog. Photovoltaics Res. Appl. 23 (2015) 705–716.

[54] M. Bär, A. Ennaoui, J. Klaer, T. Kropp, R. Sáez-araoz, S. Lehmann, A. Grimm, I. Lauermann, C. Loreck, S. Sokoll, H.-W. Schock, C.-H. Fischer, M.C. Lux-Steiner, Intermixing at the heterointerface between ZnS/Zn(S,O) bilayer buffer and $CuInS_2$ thin film solar cell absorber, J. Appl. Phys. 100 (2006) 064911.

[55] J. Bastek, N.A. Stolwijk, R. Wuerz, A. Eicke, J. Albert, S. Sadewasser, Zinc diffusion in polycrystalline $Cu(In,Ga)Se_2$ and single-crystal $CuInSe_2$ layers, Appl. Phys. Lett. 101 (2012) 074105.

[56] T. Nakada, M. Mizutani, Improved efficiency of $Cu(In,Ga)Se_2$ thin film solar cells with chemically deposited ZnS buffer layers by air-annealing-formation of homojunction by solid phase diffusion, Conf. Rec. Twenty-Eighth IEEE Photovolt. Spec. Conf. 00CH37036 (2000) 529–534.

[57] T. Nakada, Diffusion behavior and microstructural properties of the CBD-ZnS/CIGS interface boundary, Mater. Res. Soc. Symp. - Proc. 668 (2001) 1–9.

[58] T. Nakada, M. Mizutani, Improved efficiency of Cu(In,Ga)Se2 thin film solar cells with chemically deposited ZnS buffer layers by air-annealing-formation of homojunction by solid phase diffusion, Conf. Rec. Twenty-Eighth IEEE Photovolt. Spec. Conf. 00CH37036 (2000) 529–534.

[59] F. Werner, F. Babbe, J. Burkhart, C. Spindler, H. Elanzeery, S. Siebentritt, Interdiffusion and Doping Gradients at the Buffer/Absorber Interface in Thin-Film Solar Cells, ACS Appl. Mater. Interfaces. 10 (2018) 28553–28565.

[60] S. Tanuma, C.J. Powell, D.R. Penn, Calculations of electron inelastic mean free paths. IX. Data for 41 elemental solids over the 50 eV to 30 keV range, Surf. Interface Anal. 43 (2011) 689–713.

[61] R. Storn, K. Price, Differential Evolution – A Simple and Efficient Heuristic for Global Optimization over Continuous Spaces, J. Glob. Optim. 11 (1997) 341–359.

[62] P. Virtanen, R. Gommers, T.E. Oliphant, M. Haberland, T. Reddy, D. Cournapeau, E.

Burovski, P. Peterson, W. Weckesser, J. Bright, S.J. van der Walt, M. Brett, J. Wilson, K.J. Millman, N. Mayorov, A.R.J. Nelson, E. Jones, R. Kern, E. Larson, C.J. Carey, İ. Polat, Y. Feng, E.W. Moore, J. VanderPlas, D. Laxalde, J. Perktold, R. Cimrman, I. Henriksen, E.A. Quintero, C.R. Harris, A.M. Archibald, A.H. Ribeiro, F. Pedregosa, P. van Mulbregt, A. Vijaykumar, A. Pietro Bardelli, A. Rothberg, A. Hilboll, A. Kloeckner, A. Scopatz, A. Lee, A. Rokem, C.N. Woods, C. Fulton, C. Masson, C. Häggström, C. Fitzgerald, D.A. Nicholson, D.R. Hagen, D. V. Pasechnik, E. Olivetti, E. Martin, E. Wieser, F. Silva, F. Lenders, F. Wilhelm, G. Young, G.A. Price, G.L. Ingold, G.E. Allen, G.R. Lee, H. Audren, I. Probst, J.P. Dietrich, J. Silterra, J.T. Webber, J. Slavič, J. Nothman, J. Buchner, J. Kulick, J.L. Schönberger, J.V. de Miranda Cardoso, J. Reimer, J. Harrington, J.L.C. Rodríguez, J. Nunez-Iglesias, J. Kuczynski, K. Tritz, M. Thoma, M. Newville, M. Kümmerer, M. Bolingbroke, M. Tartre, M. Pak, N.J. Smith, N. Nowaczyk, N. Shebanov, O. Pavlyk, P.A. Brodtkorb, P. Lee, R.T. McGibbon, R. Feldbauer, S. Lewis, S. Tygier, S. Sievert, S. Vigna, S. Peterson, S. More, T. Pudlik, T. Oshima, T.J. Pingel, T.P. Robitaille, T. Spura, T.R. Jones, T. Cera, T. Leslie, T. Zito, T. Krauss, U. Upadhyay, Y.O. Halchenko, Y. Vázquez-Baeza, SciPy 1.0: fundamental algorithms for scientific computing in Python, Nat. Methods. 17 (2020) 261–272.